

**Synthesis of 2D/2D CoAl-LDHs/Ti<sub>3</sub>C<sub>2</sub>T<sub>x</sub> Schottky-junction with enhanced interfacial charge transfer and visible-light photocatalytic performance**

Binbin Shao <sup>a</sup>, Zhifeng Liu <sup>a,\*</sup>, Guangming Zeng <sup>a,\*</sup>, Yang Liu <sup>a</sup>, Qinghua Liang <sup>a</sup>, Qingyun He <sup>a</sup>, Ting Wu <sup>a</sup>, Yuan Pan <sup>a</sup>, Jing Huang <sup>a</sup>, Zan Peng <sup>a</sup>, Songhao Luo <sup>a</sup>, Chao Liang <sup>a</sup>, Xiaojuan Liu <sup>b</sup>, Shehua Tong <sup>a</sup>, Jie Liang <sup>a</sup>

<sup>a</sup> College of Environmental Science and Engineering, Hunan University and Key Laboratory of Environmental Biology and Pollution Control (Hunan University), Ministry of Education, Changsha 410082, P.R. China

<sup>b</sup> The First Affiliated Hospital of Hunan University of Chinese Medicine, Changsha 410007, P.R. China

\* Corresponding authors at:

<sup>a</sup> College of Environmental Science and Engineering, Hunan University and Key Laboratory of Environmental Biology and Pollution Control (Hunan University), Ministry of Education, Changsha 410082, P.R. China

E-mail: [zhifengliu@hnu.edu.cn](mailto:zhifengliu@hnu.edu.cn) (Z. Liu)

E-mail: [zgming@hnu.edu.cn](mailto:zgming@hnu.edu.cn) (G. Zeng)

## Abstract

The layered double hydroxides (LDHs) are potential non-noble metal photocatalysts. Unfortunately, the intrinsic activity of bulk LDHs is relatively low, which limits their use. Herein, the ultrathin, porous and vacancy-rich CoAl-LDHs nanosheets were prepared by exfoliation strategy. Then, they were assembled with the early transition-metal carbides nanosheets (MXenes,  $\text{Ti}_3\text{C}_2\text{T}_x$ ) to afford a hybrid 2D/2D CoAl-LDHs/ $\text{Ti}_3\text{C}_2\text{T}_x$  photocatalyst via electrostatic assembly process. The experiments indicated that the CoAl-LDHs/ $\text{Ti}_3\text{C}_2\text{T}_x$  hybrids performed an excellent visible-light photocatalytic activity for tetracycline hydrochloride (96.67%) degradation. Diversified characterization techniques (SEM, TEM, AFM,  $\text{N}_2$  adsorption-desorption analysis, XRD, FTIR, UV-vis DRS, photoelectrochemical test) and density functional theory calculations (electronic and optical properties) have indicated that such excellent photocatalytic activity was ascribed to the synergy and the Schottky heterojunction formation between CoAl-LDHs nanosheets and  $\text{Ti}_3\text{C}_2\text{T}_x$  nanosheets, which possessed markedly visible-light absorption, high specific surface area, rapid electrons transfer and depressed electron-hole pairs recombination.

**Keywords:** Ultrathin layered double hydroxides; Vacancy-rich; MXenes; Schottky junction; Density functional theory

## 1. Introduction

Photocatalysis has received increasing attention in solving environmental contaminants, such as dyes, antibiotics, phenols, volatile organic compounds (VOCs), heavy metals etc., due to their eco-friendly and high-efficiency nature [1-4]. To date, numerous semiconductor materials have been researched for environment remediation, including  $\text{TiO}_2$ ,  $\text{CdS}$ ,  $\text{BiVO}_4$ ,  $\text{Ag}_3\text{PO}_4$ ,  $\text{g-C}_3\text{N}_4$ ,  $\text{ZnIn}_2\text{S}_4$ , MOFs, etc. [5-7]. However, although these photocatalysts performed a considerable photocatalytic activity for the removal of various contaminants, it is still hard to apply them in practical because of some stubborn disadvantages among them, for instance, the low specific surface area, the weak photostability, the high cost, the fast recombination of photoinduced carriers [8, 9]. Therefore, it is still a research hotspot to explore a suitable photocatalyst with good practical application potential.

In recent years, layered double hydroxides (LDHs), as a kind of two-dimensional (2D) laminated materials, have been applied extensively in the field of catalysis due to the easily prepared strategy and low cost. Besides, the LDHs possess large surface area, flexible interlayer structure for electron transfer, visible-light (VSL) response performance, abundant active sites, which endow them great potential application in photocatalysis [8, 10]. The LDHs with the general expression of  $[\text{M}_{1-x}^{2+}\text{M}_x^{3+}(\text{OH})_2](\text{A}^{n-})^{x/n} \cdot m\text{H}_2\text{O}]$ , where  $\text{M}^{2+}$  and  $\text{M}^{3+}$  are divalent metals ( $\text{Ca}^{2+}$ ,  $\text{Mg}^{2+}$ ,  $\text{Ni}^{2+}$ ,  $\text{Zn}^{2+}$  or  $\text{Co}^{2+}$  etc.) and trivalent metals ( $\text{Al}^{3+}$ ,  $\text{Fe}^{3+}$  etc.), respectively, and  $\text{A}^{n-}$  represents a charge-balancing anion, typically is the  $\text{CO}_3^{2-}$  [10]. In the last few years,

several LDHs have been studied in photocatalysis, such as NiAl-LDHs, CoAl-LDHs, MgAl-LDHs, ZnTi-LDHs and so on [10, 11]. However, the previous studies indicated that although the LDHs materials possess a certain VSL photocatalytic activity, the pristine LDHs generally suffer poor photocatalytic performance because of the low migration of charge, the fast recombination of photoinduced electron-hole ( $e^-h^+$ ) pairs, the dissatisfactory morphology and structural characteristics etc. [12]. Thus, a number of researchers have moved towards improving the photocatalytic activity of LDHs-based materials through designing morphology and dimension, creating surface vacancies, and constructing composites with other materials [8, 12]. By designing morphology and dimension of LDHs-based materials, the bulk LDHs could be prepared into ultrathin LDHs nanosheets, which is usually obtained by exfoliation. Compared to the bulk LDHs, the exfoliated LDHs nanosheets possess a larger specific surface area and more active sites. Meanwhile, it is more likely to create surface vacancies on the exfoliated LDHs. The surface vacancies (such as oxygen vacancies, metal vacancies) could cause new energy levels to diminish the band gap thus improving VSL response, as well as could act as the charge transfer adsorption sites to suppress photogenerated  $e^-h^+$  pairs recombination [13, 14]. These optimization measures could markedly promote the photocatalytic performance of the LDHs. For instance, Zou et al. [11] had synthesized the ZnTi-LDH nanosheets contained abundant oxygen vacancies, which could be as a high-efficiency photocatalyst for selective oxidation of benzyl alcohol to benzaldehyde under VSL irradiation. As for constructing composites, many related studies also have been done, and diverse

materials have been combined with LDHs to build composite photocatalysts, including noble metal nanoparticles, semiconductor materials and carbon materials [10, 15]. For example, Wang et al. [15] found that the photocatalytic activity of MgAl-LDHs for the selective oxidation of benzyl alcohol to benzaldehyde under VSL irradiation could be significantly enhanced when loaded the Au-Pd bimetallic alloy nanoparticles on the surface of MgAl-LDHs. Wu et al. [10] found that O-doped g-C<sub>3</sub>N<sub>4</sub>/CoAl-LDHs composite exhibited excellent VSL photodegradation activity for dye removal. The construction of composites could give play to the advantages of diversified materials, and the internal electric field could be formed between different materials to accelerate the transfer of carriers, then boosting the photocatalytic activity of composites.

In addition to the common materials mentioned above, recently, a new group of 2D nanostructure materials, namely, the early transition-metal carbides and nitrides (MXenes), have received increasing attentions because of the excellent electrical conductivity, hydrophilic, sufficient reactive sites, adjustable structure, and so on. The first discovery of MXene (Ti<sub>3</sub>C<sub>2</sub>) was in 2011, and they are often prepared via etching out the A layers from MAX phase (M represents transition metal, A represents group IIIA/IVA element and X represents C and/or N element) with strong acid (such as HF or LiF/HCl) and the subsequent exfoliation processes [16-18]. MXenes possess a universal equation: M<sub>n+1</sub>X<sub>n</sub>T<sub>x</sub> (n=1-3, T<sub>x</sub> represents the surface termination groups, eg. -O, -F and -OH) [18, 19]. Many previous studies and density functional theory (DFT) calculation indicated that the surface terminations strongly affect the work function of

MXenes, inducing the MXenes more viable as heterogeneous catalysts range from metallic to semiconducting, and they also could serve as the anchor sites for further modifications with materials [20-22]. Up to now, more than 20 MXenes, including  $\text{Ti}_2\text{CT}_x$ ,  $\text{Ti}_3\text{C}_2\text{T}_x$ ,  $\text{Nb}_2\text{CT}_x$ ,  $\text{V}_2\text{CT}_x$ ,  $\text{Ti}_3\text{CNT}_x$  and  $\text{Ta}_4\text{C}_3\text{T}_x$  etc. have been reported [17], and they exhibit great application potential in energy storage, electromagnetic interference shielding, sensors, photothermal conversion, electrocatalytic and photocatalytic fields [17, 20, 23, 24]. Previous studies proved that the photocatalytic performance would increase markedly when decorated semiconductor photocatalysts with MXenes. For instance, Su et al. [25] reported that the  $\text{Ti}_3\text{C}_2/\text{g-C}_3\text{N}_4$  heterojunction performed a 10 times higher photocatalytic  $\text{H}_2$  evolution activity than that of  $\text{g-C}_3\text{N}_4$ . Cai et al. [26] reported that  $\text{Ti}_3\text{C}_2$  could significantly increase the photocatalytic performance and stability of  $\text{Ag}_3\text{PO}_4$  for the degradation of several organic contaminants. Furthermore, some recent studies have also shown that the MXenes could significantly improve the performance of LDHs, thus expanding their application potential in fields such as electrocatalysis, supercapacitor, sensor, battery and so on [27-30]. However, to date, there was still a lack of study on MXenes/LDHs composites in photocatalysis.

In this work, we reported the preparation of ultrathin, porous and vacancy-rich CoAl-LDHs nanosheets by exfoliation strategy. Meanwhile, the composite of CoAl-LDHs nanosheets/ $\text{Ti}_3\text{C}_2\text{T}_x$  MXenes also had been fabricated via an electrostatic assembly process (the negatively charged  $\text{Ti}_3\text{C}_2\text{T}_x$  MXenes and the positively charged CoAl-LDHs nanosheets [31]). Then, the VSL photocatalytic performance of the

synthesized photocatalysts was estimated toward the photodegradation of tetracycline hydrochloride. Multiple techniques were introduced to study their composition, morphology, and photoelectric characteristics (SEM, TEM, AFM, XRD, FTIR, XPS, N<sub>2</sub> adsorption-desorption analysis, UV-vis DRS, PL, photoelectrochemical test). Furthermore, the electronic and optical properties (such as band structures, density of states, effective mass of electron, dielectric function, loss function, conductivity, work function and so on) of photocatalysts were investigated by DFT calculation. Experimental and theoretical results manifested that the nanohybrids performed superior VSL photocatalytic performance. This work would open a new facile path for preparing the efficient LDHs-based composites, and can be hopefully applied in photocatalysis, photoelectrochemical devices and so on.

## **2. Experimental**

### **2.1. Synthesis of photocatalysts**

The CoAl-LDHs nanosheets were prepared according to the follow steps: in details, 0.015 M of Co(NO<sub>3</sub>)<sub>2</sub>·6H<sub>2</sub>O, 0.005 M of Al(NO<sub>3</sub>)<sub>3</sub>·9H<sub>2</sub>O and 0.05 M of urea were added into 70 mL of ultrapure water, and continuous stirring for 1 h at room temperature to get a mixture. Then, the mixture was treated by hydrothermal reaction at 120 °C for 24 h, finally, the bulk CoAl-CO<sub>3</sub><sup>2-</sup>-LDHs were obtained. Subsequently, an anion exchange process was performed, namely, 0.5 g of CoAl-CO<sub>3</sub><sup>2-</sup>-LDHs was added into 500 mL of aqueous solution, which contained NaNO<sub>3</sub> (0.75 M) and HNO<sub>3</sub> (3 mM). The mixture was sealed after deoxidation with N<sub>2</sub> gas, and stirred 48 h to

convert the  $\text{CoAl-CO}_3^{2-}$ -LDHs into  $\text{CoAl-NO}_3^-$ -LDHs form. Follow this, the exfoliation process was performed by dispersing 0.5 g of  $\text{CoAl-NO}_3^-$ -LDHs in 500 mL of formamide, the mixture was then sealed after deoxidation and vigorously stirred for 24 h to get the exfoliated  $\text{CoAl-LDHs}$  nanosheets suspension, then the  $\text{CoAl-LDHs}$  nanosheets (CAL) suspension was obtained by centrifugation (10,000 rpm, 10 min) and redispersed in deoxidized ultrapure water, the concentration was determined (about  $1.0 \text{ mg mL}^{-1}$ ) [32].

The preparation process of  $\text{Ti}_3\text{C}_2\text{T}_x$  MXenes had been reported in our previous study [22]. The obtained few-layer or single  $\text{Ti}_3\text{C}_2\text{T}_x$  nanosheets (TCT) suspension was about  $2.0 \text{ mg mL}^{-1}$ .

The  $\text{CoAl-LDHs/Ti}_3\text{C}_2\text{T}_x$  composites were prepared as follows: a certain amount of  $\text{Ti}_3\text{C}_2\text{T}_x$  nanosheets suspension (1.0 mL, 2.5 mL, 5.0 mL, 7.5 mL, 10.0 mL) was added to 100 mL of  $\text{CoAl-LDHs}$  nanosheets suspension dropwise, and continuous stirring for 3 h at room temperature under  $\text{N}_2$  flow. Then, the  $\text{CoAl-LDHs/Ti}_3\text{C}_2\text{T}_x$  composites were obtained by vacuum filtration and finally dried in a vacuum oven overnight. The nominal weight ratios of  $\text{Ti}_3\text{C}_2\text{T}_x$  to  $\text{CoAl-LDHs}$  were 2, 5, 10, 15 and 20 wt% (CAL/TCT-2, CAL/TCT-5, CAL/TCT-10, CAL/TCT-15, CAL/TCT-20), respectively. The schematic illustration of the synthesis process for the  $\text{CoAl-LDHs/Ti}_3\text{C}_2\text{T}_x$  composite was displayed in Fig. 1. The related information of Materials and Characterization had been showed in the supplementary information.



## 2.2. Theoretical calculations

The CASTEP method was employed for the DFT calculations, and the exchange-correlation function was set as GGA-PBE. Meanwhile, the spin-polarized Hubbard DFT+U was applied to for all optimizations, and the value of U was 3.52 eV for Co. Energy cutoff, SFC tolerance and k-point were set 340 eV,  $2 \times 10^{-6}$  eV atom<sup>-1</sup> and  $3 \times 3 \times 1$ , respectively. A  $4 \times 4 \times 1$  supercell was adopted for the CoAl-LDHs and Ti<sub>3</sub>C<sub>2</sub>O<sub>2</sub> model (The model of Ti<sub>3</sub>C<sub>2</sub>O<sub>2</sub> was chosen for Ti<sub>3</sub>C<sub>2</sub>T<sub>x</sub> calculation). The model of O-defective CoAl-LDHs, Co-defective CoAl-LDHs and O&Co-defective CoAl-LDHs were built based on the perfect CoAl-LDHs. The O&Co-defective CoAl-LDHs/Ti<sub>3</sub>C<sub>2</sub>O<sub>2</sub> model was constructed by placing Ti<sub>3</sub>C<sub>2</sub>O<sub>2</sub> model 3 Å above the O&Co-defective CoAl-LDHs to form a heterogeneous structure. The ionic cores were set as ultrasoft pseudopotentials to promote transferability and decrease the number of plane waves needed in the expansion of the Kohn-Sham orbitals [32]. A more than 15 Å vacuum space was introduced to avoid the interference interaction between the neighboring systems.

## 2.3. Photocatalytic test

The photocatalytic activity of the prepared photocatalysts was evaluated toward the photodegradation of 10 mg L<sup>-1</sup> of tetracycline hydrochloride (TCH). Namely, 100 mg of samples were dispersed in 100 mL of TCH. Before irradiation, a 60 min dark adsorption test was carried out to attain adsorption-desorption equilibrium. Subsequently, the photocatalytic test was implemented under the VSL irradiation for

60 min (a 300W Xenon lamp (PLS-SXE300, Perfectlight corporation, Beijing) was served as the photo source,  $\lambda > 420$  nm, the average visible light intensity was ca. 100 mW cm<sup>-2</sup> measured by a light meter (HS1010)). The cycle experiments were carried out as follows: the reaction solution in the photocatalytic system was removed by centrifugation (8000 rpm, 5 min) after the completion of one-stage photocatalytic experiment, and then the residual photocatalyst was re-dispersed in 100 mL of TCH for the next photocatalytic experiment. In each photocatalysis process, 1 mL of mixture was sucked out and filtrated for concentration determination at intervals [33].

### 3. Results and discussion

#### 3.1. Morphology structure

The morphology of prepared photocatalysts was studied by FESEM, TEM and AFM measures. As shown in FESEM images, obviously, the Ti<sub>3</sub>AlC<sub>2</sub> was a block structure before the etching (Fig. 2A). However, a beautiful accordion-like lamellar structure of multilayered Ti<sub>3</sub>C<sub>2</sub>T<sub>x</sub> emerged after the aluminum layer was etched out (Fig. 2B). Further, the delaminated Ti<sub>3</sub>C<sub>2</sub>T<sub>x</sub> was acquired through the ultrasonication exfoliation of the multilayered Ti<sub>3</sub>C<sub>2</sub>T<sub>x</sub>, resulting in the forming of few-layer or single Ti<sub>3</sub>C<sub>2</sub>T<sub>x</sub> sheets (Fig. 2C). These results were highly consistent with previous study [20]. As for the CoAl-LDHs, the bulk CoAl-LDHs showed the laminated structure with a smooth surface (Fig. 2E). However, after mechanical exfoliation, the CoAl-LDHs became ultrathin nanosheets, and their surface was no longer smooth, which might be due to the forming of more porous structures in the exfoliation

process (Fig. 2F). Furthermore, according to TEM and HRTEM analysis, it was obvious that the exfoliated CoAl-LDHs were irregular strip-shaped nanosheet structure, and there were rich pores distributed on the surface of CoAl-LDHs sheets (Fig. 2I, J), which could provide more active sites for the reactants, then enhancing the photocatalytic activity of the photocatalyst. Further, the HRTEM images revealed that the lattice spacing of 0.260 nm corresponded to the (012) plane of CoAl-LDHs [8], meanwhile, the local lattice distortions were obvious in HRTEM images, which could be due to the generation of vacancies (Fig. 2G, H), some previous studies had also reported the similar phenomenon [13, 32]. For the delaminated  $\text{Ti}_3\text{C}_2\text{T}_x$ , the TEM image showed that they were random nanosheets, which contained three or four layers of monolayer  $\text{Ti}_3\text{C}_2\text{T}_x$  sheets (Fig. 2D). Besides, the HRTEM image indicated that the lattice spacing of 0.216 nm should correspond to the (002) plane of  $\text{Ti}_3\text{C}_2\text{T}_x$  (Fig. 2H), meanwhile, some disordered lattices also had been found, which should be due to the existence of carbon material in the  $\text{Ti}_3\text{C}_2\text{T}_x$  [9]. As for the CALTCT-15, it was clear that the CoAl-LDHs nanosheets were decorated with some other sheets, which should be the  $\text{Ti}_3\text{C}_2\text{T}_x$  sheets (Fig. 2K). Meanwhile, it could be found that there are two types of contrast fringes in the HRTEM image of CALTCT-15 nanohybrid (Fig. 2L). In addition, the AFM analysis (Fig. 3A) further reveal that the diameter of CoAl-LDHs nanosheets up to micron scale, and their apparent thickness was determined to be about 3.2 nm, which was about consistent with four layers of CoAl-LDHs nanosheets (the thickness of a single CoAl-LDHs layer was about 0.756 nm according to the XRD result), and they were much thinner than the unexfoliated CoAl-LDHs (24-34

nm, about 32-45 layers (Fig. S1)). For  $\text{Ti}_3\text{C}_2\text{T}_x$  sheets (Fig. 3B), they were nanoscale in diameter, and the thickness of  $\text{Ti}_3\text{C}_2\text{T}_x$  sheets were about 5.1 nm, indicating that the  $\text{Ti}_3\text{C}_2\text{T}_x$  sheets were about three layers, however, the thickness of multilayered  $\text{Ti}_3\text{C}_2\text{T}_x$  reached to 60-100 nm (about 40-67 layers (Fig. S2)) [34]. As for the CALTCT-15 (Fig. 3C), obviously, the lower height of 3.5 nm should be assigned to the CoAl-LDHs nanosheets, while the higher height of 5.1 nm could be ascribed to  $\text{Ti}_3\text{C}_2\text{T}_x$  nanosheets. This result revealed that  $\text{Ti}_3\text{C}_2\text{T}_x$  sheets “face-to-face” decorated on the surface of CoAl-LDHs nanosheets, and the combination of the two nanosheets had no significant effect on their thickness. These AFM results were very close to previous reports and verified the few-layered nanosheet structure of prepared photocatalysts [32]. Further, the element composition and distribution were further studied by the EDS analysis and elemental mapping. The EDS characterization showed the composition of each element, and the results were displayed in Table 1. Obviously, the Co/Al ratio (2.6:1) in bulk CoAl-LDHs was close to that in the synthesis mixture (3:1), while the ratio in CoAl-LDHs nanosheets was only 1.51:1, suggesting the rich Co vacancies were produced during the mechanical exfoliation process [32]. Meanwhile, the relative content of O was also decreased after the exfoliation process, suggesting the O vacancies also existed, the similar phenomena had also been observed in some previous studies [32]. Furthermore, the EPR results also verified that the O vacancies were existed in the CoAl-LDHs nanosheets. As displayed in Fig. 4A, compared with bulk CoAl-LDHs, the CoAl-LDHs nanosheets performed distinctly increased EPR signal at  $g = 2.000$ , corresponding to the electrons

captured by O vacancies [35]. As for the CALTCT-15, the Co/Al ratio in CALTCT-15 (1.46:1) was close to that of in CoAl-LDHs nanosheets, however, the content of C was increased due to the introduction of  $\text{Ti}_3\text{C}_2\text{T}_x$ . Furthermore, the elemental mapping displayed the Al, Co, O, Ti, and C elements were uniformly distributed in composite (Fig. 2). The above results confirmed that the ultrathin CoAl-LDHs nanosheets,  $\text{Ti}_3\text{C}_2\text{T}_x$  and CoAl-LDHs/ $\text{Ti}_3\text{C}_2\text{T}_x$  2D/2D nanohybrids were successfully prepared, meanwhile, the CoAl-LDHs nanosheets possess abundant pores and vacancies.

The surface area and porosity of photocatalysts perform a significant part in their photocatalytic activity. As displayed in the  $\text{N}_2$  adsorption-desorption isotherms (Fig. 4B), the type-IV isotherm with an H3 hysteresis loop existed in all samples, which demonstrated the presence of mesoporous structure in these photocatalysts [10]. In details, the average pore size, pore volume and specific surface area of the samples were showed in Table 2 and Fig. S3A. The average pore diameters of  $\text{Ti}_3\text{C}_2\text{T}_x$  nanosheets, CoAl-LDHs nanosheets and CALTCT-15 nanohybrids were 2.520 nm, 3.372 nm and 4.726 nm, respectively, the pore volume were  $0.014 \text{ cm}^3 \text{ g}^{-1}$ ,  $0.162 \text{ cm}^3 \text{ g}^{-1}$  and  $0.203 \text{ cm}^3 \text{ g}^{-1}$ , respectively, and the specific surface area were  $4.502 \text{ m}^2 \text{ g}^{-1}$ ,  $36.546 \text{ m}^2 \text{ g}^{-1}$  and  $51.098 \text{ m}^2 \text{ g}^{-1}$ , respectively. Compared with the  $\text{Ti}_3\text{C}_2\text{T}_x$  and CoAl-LDHs, the CALTCT-15 nanohybrids possesses higher specific surface area and mesoporous features, which could promote the exposure of the active sites, and the diffusion of contaminants and active substances during the photocatalytic process, thus improving the photocatalytic performance of CALTCT-15 nanohybrids.

### 3.2. Crystal and chemical structure

The XRD results of obtained photocatalysts were presented in Fig. 4C. Obviously, after  $\text{Ti}_3\text{AlC}_2$  was etched by acid solution, the characteristic peaks at  $6.9^\circ$ ,  $18.8^\circ$ ,  $29.5^\circ$ ,  $44.3^\circ$  and  $61.9^\circ$  were assigned to the (002), (004), (006), (105) and (110) reflection of  $\text{Ti}_3\text{C}_2\text{T}_x$ , respectively [36]. The (002) at  $7.8^\circ$  and (004) at  $19.2^\circ$  of  $\text{Ti}_3\text{AlC}_2$  were widened and moved to lower angle side (Fig. S3B), signifying the elimination of Al interlayer and the developing of  $\text{Ti}_3\text{C}_2\text{T}_x$  nanosheets [5, 37]. For the CoAl-LDHs nanosheets, the diffraction peaks appeared at  $2\theta = 11.7^\circ$ ,  $24.0^\circ$ ,  $34.8^\circ$ ,  $39.2^\circ$  and  $46.9^\circ$  were agreed with the (003), (006), (009), (012) and (018) lattice planes of the pure CoAl-LDHs reference (PDF-#38-0487) [10]. Thus, the interlayer distance ( $d_{003}$ ) of CoAl-LDHs nanosheets was about 0.756 nm based on the formula of  $2d\sin\theta=n\lambda$  (where  $d$  represents the  $d_{003}$ ,  $n=1$ ,  $\lambda=0.15406$  nm), and the gallery height was about 0.279 nm (brucite-like layer thickness was 0.477 nm) [38]. According to the XRD patterns of five nanohybrids, both of  $\text{Ti}_3\text{C}_2\text{T}_x$  and CoAl-LDHs nanosheets dominating phases were existed, and the characteristic peak strength changes with the change of content. The above results demonstrated that the two materials were well combined, and the introduction of  $\text{Ti}_3\text{C}_2\text{T}_x$  did not affect the phase of CoAl-LDHs.

The typical functional groups of the obtained photocatalysts were investigated through FTIR analysis. As showed in Fig. 4D, The absorption at  $2366\text{ cm}^{-1}$  for all samples ascribed to the antisymmetric C=O stretching, which due to the atmospheric  $\text{CO}_2$  [39]. For the  $\text{Ti}_3\text{C}_2\text{T}_x$  nanosheets, the peak at  $3442\text{ cm}^{-1}$  was mainly ascribed to the -OH which terminated on the  $\text{Ti}_3\text{C}_2\text{T}_x$  and water molecules and -OH group [1, 40].

The bands at 1647  $\text{cm}^{-1}$ , 1335  $\text{cm}^{-1}$ , 1049  $\text{cm}^{-1}$ , 895  $\text{cm}^{-1}$  and 559  $\text{cm}^{-1}$  correspond to the stretching vibration modes of C=O, C-C, C-Ti, C-F and Ti-O groups grafted onto  $\text{Ti}_3\text{C}_2\text{T}_x$ , respectively [18, 41]. For the CoAl-LDHs nanosheets, the broad peak centered at 3440  $\text{cm}^{-1}$  corresponds to the O-H stretching vibration of interlayer  $\text{H}_2\text{O}$  and H-bonded -OH group [42]. The peak at 1552  $\text{cm}^{-1}$  was indicative of the H-O-H ( $\delta\text{-H}_2\text{O}$ ) deformation vibration [43]. The peaks at 1354  $\text{cm}^{-1}$ , 837  $\text{cm}^{-1}$  and 977  $\text{cm}^{-1}$  were due to the  $\nu_3$  stretching vibration and the bending modes of  $\text{CO}_3^{2-}$  [40, 43]. The troughs located in the low-frequency region (550-810  $\text{cm}^{-1}$ ) were generally corresponded to the stretching and bending vibration of M-O, O-M-O and M-O-M the crystals [8]. As for the CoAl-LDHs/ $\text{Ti}_3\text{C}_2\text{T}_x$  nanohybrids, they had the homologous FTIR spectrum as the CoAl-LDHs, which could due to the fact that there was a small amount of  $\text{Ti}_3\text{C}_2\text{T}_x$  in the nanohybrids. The FTIR results verified that the composites had abundant functional groups, contributing to improve the photocatalytic activity.

For determining the surface chemical composition and valence state of the samples, XPS analysis was introduced. Based on the XPS survey spectra (Fig. 5A), the  $\text{Ti}_3\text{C}_2\text{T}_x$  nanosheets mainly composed of Ti, C, O elements, the CoAl-LDHs nanosheets mainly contained Co, Al, O elements, and the CALTCT-15 nanohybrids contained Ti, Co, Al, C, O elements, demonstrating the composites were successfully fabricated. Furthermore, the high-resolution XPS spectra of Ti 2p, Co 2p, Al 2p, O 1s and C 1s were revealed. As displayed in Fig. 5B and Fig. S4A, the Ti 2p spectra of  $\text{Ti}_3\text{C}_2\text{T}_x$  nanosheets and CALTCT-15 nanohybrids included six characteristic peaks. The binding energy at 454.4 eV (455.1 eV), 455.7 eV (457.5 eV), 458.0 eV (458.4 eV),

459.8 eV (460.0 eV), 462.0 eV (461.8 eV), 464.1 eV (464.1 eV), corresponded to Ti-C 2p<sub>3/2</sub>, Ti<sup>2+</sup> 2p<sub>3/2</sub>, Ti-O 2p<sub>3/2</sub>, Ti-C 2p<sub>1/2</sub>, Ti<sup>2+</sup> 2p<sub>1/2</sub>, Ti-O 2p<sub>1/2</sub>, respectively. [5, 44]. Compared with Ti<sub>3</sub>C<sub>2</sub>T<sub>x</sub> nanosheets, the position of characteristic peaks in CALTCT-15 nanohybrids had some changes, which should be due to the presence of CoAl-LDHs nanosheets. We could know from the Co 2p spectra (Fig. S4B and Fig. 5C) that there were eight characteristic peaks in bulk CoAl-LDHs, CoAl-LDHs nanosheets and CALTCT-15 nanohybrids [44-46]. In bulk CoAl-LDHs (CoAl-LDHs nanosheets), the peaks at 781.7 eV (781.3 eV) and 797.9 eV (797.7 eV) represented Co<sup>3+</sup> 2p<sub>3/2</sub> and 2p<sub>1/2</sub>, the peaks at 783.3 eV (783.1 eV) and 799.5 eV (799.7 eV) indicated Co<sup>2+</sup> 2p<sub>3/2</sub> and 2p<sub>1/2</sub>, and the corresponding satellite peaks presented at 787.3 eV (786.5 eV) and 803.4 eV (803.7 eV) for Co<sup>3+</sup>, and the corresponding satellite peaks presented at 790.5 eV (789.7 eV) and 805.9 eV (806.1 eV) for Co<sup>2+</sup>. As for the CALTCT-15 nanohybrids, the peaks at 781.3 eV and 797.6 eV represented Co<sup>3+</sup> 2p<sub>3/2</sub> and 2p<sub>1/2</sub>, the peaks at 783.5 eV and 803.1 eV indicated Co<sup>2+</sup> 2p<sub>3/2</sub> and 2p<sub>1/2</sub>. Furthermore, the corresponding satellite peaks located at 787.3 eV and 807.1 eV for Co<sup>3+</sup>, and the corresponding satellite peaks located at 791.6 eV and 813.6 eV for Co<sup>2+</sup>. Furthermore, the existence of Co vacancies might be further confirmed by the Co content based on XPS results as some previous studies had reported (Fig. S4B) [47-50]. Firstly, the rough atomic percent of Co in CoAl-LDHs could be determined by XPS spectra, the results indicated that the percent of Co in the bulk CoAl-LDHs (39.83%) was higher than that of in CoAl-LDHs nanosheets (30.76%), which was consistent with the EDS results, indicating the existence of Co vacancies [47, 48].



Meanwhile, the area ratio of  $\text{Co}^{2+}$  and  $\text{Co}^{3+}$  peaks for CoAl-LDHs nanosheets was 0.52, obviously lower than that of bulk CoAl-LDHs (0.64), which also confirms the presence of Co vacancies in CoAl-LDHs nanosheets [49, 50]. Fig. 5D and Fig. S4C revealed the characteristic binding energy peak of Al 2p at 74.0 eV and 73.9 eV for CoAl-LDHs and CALTCT-15, respectively, indicating that Al was the +3 oxidation state in the form of Al-OH [38]. The O 1s showed in Fig. 5E and Fig. S4D, E, it is observed that the O 1s for CoAl-LDHs could be fitted to four characteristic peaks at 530.2 eV, 531.2 eV, 532.2 eV and 533.6 eV, corresponded to the Co/Al-O, O vacancies, hydroxyl bonding and adsorbed  $\text{H}_2\text{O}$ , respectively [35, 51]. For the  $\text{Ti}_3\text{C}_2\text{T}_x$ , there were three characteristic peaks at 529.2 eV, 530.8 eV and 532.5 eV, which were assigned to Ti-O, Ti-C-O and Ti-OH bonds, respectively [52, 53]. Compared to two pure single materials, the O 1s of CALTCT-15 included five characteristic peaks at 527.8 eV, 530.0 eV, 531.1 eV, 532.4 eV and 533.6 eV, corresponded to the Ti-O, the Co/Al-O, O vacancies, hydroxyl bonding and adsorbed  $\text{H}_2\text{O}$ , respectively. As showed in Fig. 5F and Fig. S4F, the C 1s spectra of  $\text{Ti}_3\text{C}_2\text{T}_x$  nanosheets was deconvoluted into four speaks at 280.9 eV (C-Ti), 284.4 eV (C-C), 285.4 eV (C-O) and 286.1 eV (C=O) [9, 54]. As for the CALTCT-15 nanohybrids, there were five peaks at 280.0 eV, 282.3 eV, 284.2 eV, 285.7 eV and 286.4 eV, which were ascribed to C-Ti, C-Ti-O, C-C, C-O and C=O, respectively [9, 44]. Therefore, the XPS results further affirmed the co-existence of CoAl-LDHs and  $\text{Ti}_3\text{C}_2\text{T}_x$  in the CALTCT-15 nanohybrids, meanwhile, the existence of O and Co vacancies also could be confirmed according to the XPS results.

### 3.3. Photocatalytic performance

The photocatalytic performance of the obtained photocatalysts was evaluated via the photodegradation of TCH under VSL irradiation. Before the photodegradation test, a 60 min dark adsorption test was carried out to attain adsorption-desorption equilibrium. As showed in Fig. 6A, compared to the  $\text{Ti}_3\text{C}_2\text{T}_x$  and CoAl-LDHs nanosheets, the CoAl-LDHs/ $\text{Ti}_3\text{C}_2\text{T}_x$  nanohybrids performed preferable adsorption capacity for pollutants removal, and the maximum adsorption removal efficiency was 13.54%. The improved adsorption performance of CoAl-LDHs/ $\text{Ti}_3\text{C}_2\text{T}_x$  nanohybrids could attribute to the high surface area and porosity of the nanohybrids, meanwhile, the oxygenated groups on  $\text{Ti}_3\text{C}_2\text{T}_x$  could further enhance pollutant adsorption, then enhancing the photocatalytic activity of photocatalysts. Under VSL irradiation (Fig. 6B), obviously, the CoAl-LDHs nanosheets showed the better photocatalytic performance for TCH removal compared with the bulk CoAl-LDHs, which could be attributed to the forming of rich vacancies and porous structure in the CoAl-LDHs nanosheets. Furthermore, after the introduction of  $\text{Ti}_3\text{C}_2\text{T}_x$ , the CoAl-LDHs/ $\text{Ti}_3\text{C}_2\text{T}_x$  samples performed the superior photocatalytic activity for TCH removal compared with the single-phase, and they were in the order of CALTCT-15 (96.67%) > CALTCT-20 (94.10%) > CALTCT-10 (90.45%) > CALTCT-5 (79.80%) > CALTCT-2 (75.80%) > CoAl-LDHs (50.46%) > bulk CoAl-LDHs (32.64%) >  $\text{Ti}_3\text{C}_2\text{T}_x$  (19.54%) (Table S1). Noticeably, an excess of  $\text{Ti}_3\text{C}_2\text{T}_x$  nanosheets could cause negative influence on the photocatalytic activity, which should be due to the light shielding effect [55]. Thus, the control over the ratio of  $\text{Ti}_3\text{C}_2\text{T}_x$  nanosheets to CoAl-LDHs

nanosheets was vital to attain optimal photocatalytic activity of the nanohybrid. Meanwhile, according to the rate constant ( $k$ ) based on the pseudo-first-order kinetic model (Fig. S5A, and Table S1), the CALTCT-15 nanohybrids performed the highest removal rate for TCH. Compared with the single-phase photocatalysts, the improved photocatalytic activity for nanohybrids should be due to the synergistic effect between  $\text{Ti}_3\text{C}_2\text{T}_x$  nanosheets and CoAl-LDHs nanosheets. Furthermore, the photocatalytic performance of CALTCT-15 nanohybrids was further estimated toward the photodegradation of other two typical antibiotics (ciprofloxacin hydrochloride (CFH), sulfamethazine (SAZ)), the results showed that the CALTCT-15 sample performed the lower photocatalytic removal efficiency for CFH and SA than that of TCH, and the maximum removal efficiency was 90.45% and 80.17% for CFH and SA, respectively (Fig. S5B), the different degradation efficiencies of TCH, CFH and SAZ in the photocatalytic system might be due to their different structures, the similar results also had been obtained in our previous study [33].

Since the pollutants would be converted to intermediates during the degradation process, thus the high removal efficiency of pollutants does not mean they have been thoroughly broken down into  $\text{CO}_2$  and  $\text{H}_2\text{O}$ . Therefore, the TOC analysis was performed over CALTCT-15 nanohybrids for determining the mineralization degree of TCH. As displayed in Fig. 6C, the removal rate of TCH was a little faster than its mineralization rate. In details, the CALTCT-15 nanohybrids performed 78.46% mineralization efficiency of TCH, under the VSL irradiation for 60 min. Thus, the TOC results had given the credible evidence to verify the good mineralization of TCH

contaminant over the CALTCT-15 nanohybrids upon VSL illumination.

The photostability of the present CALTCT-15 nanohybrids was further studied by performing the cyclic tests for the photocatalytic degradation of TCH (Fig. 6D). Consequently, the CALTCT-15 nanohybrids retained about 83.16% activity for TCH degradation even after five consecutive test cycles, indicating the CALTCT-15 nanohybrids could be as a stable photocatalyst. The reduction in degradation efficiency should be due to the unavoidable loss of the photocatalyst in the cyclic experiments and the adsorption of some refractory intermediate products on the active site of photocatalyst [8]. The phase and structural stabilities of the CALTCT-15 nanohybrids were further studied through XRD analysis, obviously, the crystal structure of CALTCT-15 nanohybrids had no significant variation in the prolonged photodegradation process (Fig. 6E). Therefore, the CoAl-LDHs/Ti<sub>3</sub>C<sub>2</sub>T<sub>x</sub> nanocomposite with high photocatalytic performance would be a promising photocatalyst, and might be applied in environmental conservation in practical.

### **3.4. Optical-electrical characteristics analysis**

In order to analyze the reasons for the excellent photocatalytic activity, the optical-electrical properties of the photocatalysts had also been studied by UV-vis DRS, photoelectrochemical and photoluminescence tests. As displayed in Fig. 7A, the UV-vis DRS spectrum showed the light response property of the samples, apparently, the bulk CoAl-LDHs displayed a significant absorption for UV, while had low absorption peak in the visible region, although there was a broadband in the visible

region centered at 500 nm (due to d-d transitions of octahedral  $\text{Co}^{2+}$  within the  
 CoAl-LDHs layer) [8, 12]. Compared with the bulk CoAl-LDHs, the ultrathin  
 CoAl-LDHs nanosheets performed an improved absorption capacity for both UV and  
 visible region. The improvement should attribute to the reduction in thickness and the  
 formation of vacancies for CoAl-LDHs nanosheets, some previous similar studies had  
 also reported this phenomenon [56]. For the  $\text{Ti}_3\text{C}_2\text{T}_x$  nanosheets, it could be seen the  
 $\text{Ti}_3\text{C}_2\text{T}_x$  performed significant absorption in the range of UV and VSL, which could  
 be attributed to the black color nature of  $\text{Ti}_3\text{C}_2\text{T}_x$  [57]. As for the CoAl-LDHs/ $\text{Ti}_3\text{C}_2\text{T}_x$   
 nanohybrids, the introduction of the  $\text{Ti}_3\text{C}_2\text{T}_x$  could markedly increase the absorption  
 of VSL, and with the increase of  $\text{Ti}_3\text{C}_2\text{T}_x$  content, the absorption intensity of  
 CoAl-LDHs/ $\text{Ti}_3\text{C}_2\text{T}_x$  nanohybrids gradually increased, which was very helpful to  
 increase the VSL photocatalytic performance of the nanohybrids. Additionally, the  $E_g$   
 of the CoAl-LDHs was estimated from the Tauc's equation:  $\alpha h\nu = A(h\nu - E_g)^{n/2}$  [58].  
 According to the calculation, the  $E_g$  of bulk CoAl-LDHs and CoAl-LDHs nanosheets  
 was about 2.66 eV and 2.04 eV, respectively (Fig. 7B), which directly proved that  
 ultrathin CoAl-LDHs nanosheets possess a greater response to VSL, thus the better  
 photocatalytic performance would be performed. Tan et al. [56] also reported that the  
 $E_g$  of NiAl-LDHs could be adjusted from 2.10 eV to 1.78 eV by exfoliating bulk  
 NiAl-LDHs to monolayer NiAl-LDHs, and the reduced band gap of monolayer  
 NiAl-LDHs should be attributed to the abundant surface vacancies on monolayer  
 NiAl-LDHs. Furthermore, the potentials of conductor band (CB) and valence band  
 (VB) for CoAl-LDHs were determined by the following equations:  $E_{\text{VB}} = X - E^e + 1/2E_g$ ,

$E_{CB}=E_{VB}-E_g$ . In this study, the calculated VB and CB of bulk CoAl-LDHs was 1.61 eV and -1.05 eV, respectively, and the VB and CB of ultrathin CoAl-LDHs nanosheets are 1.30 eV and -0.74 eV, respectively. Obviously, the VB maximum was moved up, and the CB minimum was moved down, resulting in the better VSL response.

Photoelectrochemical properties had been regarded as a reliable basis for assessing the photocurrent response and the photoinduced carrier separation efficiency for the photocatalysts. As shown in Fig. 7C, the  $Ti_3C_2T_x$  sample performed a negligible amount of photocurrent, but the photocurrent intensity of CALTCT-15 nanohybrid enhanced significantly compared to that of CoAl-LDHs sample. In addition, the charge mobility was evaluated according to the arc radius in the EIS. It is commonly believed that the smaller arc in the EIS represents the less charge transfer resistance [33]. As depicted in Fig. 7D, clearly, the CALTCT-15 nanohybrid has the lowest charge migration resistance. The photocurrent and EIS results suggested that the CALTCT-15 nanohybrids exhibited the improved electron transfer process, which could be due to the existence of abundant vacancies on CoAl-LDHs nanosheets, meanwhile, the introduction of  $Ti_3C_2T_x$  could result in the forming of built-in electric field between CoAl-LDHs and  $Ti_3C_2T_x$ , thus effectively decreasing the recombination of photogenerated  $e^-h^+$  pairs and increasing the photocatalytic performance of photocatalysts [59].

The PL analysis was implemented to better comprehend the separation and migration of the photoinduced carriers of these photocatalysts (Fig. 7E). The emission peak of CALTCT-15 nanohybrid at 620 nm was lower than that of CoAl-LDHs

nanosheets, suggesting the recombination of photoinduced carriers was effectively suppressed because of the interfacial charge transfer between CoAl-LDHs and  $\text{Ti}_3\text{C}_2\text{T}_x$  [10, 60]. Meanwhile, for the CoAl-LDHs nanosheets, obviously, a shoulder peak at 648 nm and several small peaks were appeared at 640-680 nm regions, which should attribute to the forming of vacancies in the structure of CoAl-LDHs nanosheets. The previous studies indicated that the vacancies could act as luminescent sites in the photoluminescence process [13]. However, this phenomenon was not very obvious in the CALTCT-15 composite, which might be influenced by  $\text{Ti}_3\text{C}_2\text{T}_x$ . Moreover, to analyze the dynamics of carriers separation, the time-resolved PL spectrum of the photocatalysts were showed (Fig. 7F, Table S2) [12]. It could be seen that the carrier average lifetimes ( $\tau$ ) of CoAl-LDHs nanosheets and CALTCT-15 were 2.87 and 3.64 ns, respectively, indicating the addition of  $\text{Ti}_3\text{C}_2\text{T}_x$  was beneficial to restrain the recombination of photoinduced  $e^-h^+$  pairs and lengthen the carrier lifetime [10, 60].

### 3.5. Theoretical calculations

Theoretical calculation is an economical and effective method to explore the material's properties [61]. In order to further clarify the reasons for the improvement of photocatalytic performance. In this study, the optical and electronic properties of perfect CoAl-LDHs, O-defective CoAl-LDHs, Co-defective CoAl-LDHs, O&Co-defective CoAl-LDHs,  $\text{Ti}_3\text{C}_2\text{O}_2$  and O&Co-defective CoAl-LDHs/ $\text{Ti}_3\text{C}_2\text{O}_2$  composite were calculated based on the DFT. Their geometric structures and lattice parameters were showed in Fig. S6 and Table S3. The lattice types for all samples

were 3D triclinic. As is known to all, the energy levels and the  $E_g$  perform a key part in deciding the photocatalytic activity of the photocatalyst. Based on the calculation results, the  $E_g$  of perfect CoAl-LDHs was 2.62 eV (Fig. S7A), which was close to previous theoretical calculation results [36]. For the O-defective CoAl-LDHs, it was obvious that the down-shift of conduction band minimum (CBM) resulted in the decrease of  $E_g$  (2.11 eV) (Fig. S8A). However, the valence band maximum (VBM) moved up for Co-defective CoAl-LDHs, meanwhile, Co vacancies resulted in the appearance of a new vacancy level (Fig. S8B), which made the electrons to be easily excited into the CB under light irradiation [62]. As for the O&Co-defective CoAl-LDHs, the shift of band edges and the form of new vacancy level both existed (Fig. S8C). Many previous studies had also reported that the presence of vacancies would lead to the happen of these changes, which could improve the response to light and thus increasing the photocatalytic properties of the material [13, 63]. Moreover, the semiconductor type of CoAl-LDHs could be confirmed by the corresponding band structure. As displayed in Fig. S7A, the VBM and CBM of CoAl-LDHs samples were distributed at G point and Z point, respectively, manifesting the CoAl-LDHs was indirect band-gap semiconductor, and the presence of vacancy would not change the semiconductor type of CoAl-LDHs, it was consistent with the experimental result. Moreover, the band structure of  $\text{Ti}_3\text{C}_2\text{O}_2$  has also been shown in Fig. S7B. Obviously, the substantial electronic states crossing the Fermi level for  $\text{Ti}_3\text{C}_2\text{O}_2$  indicated that the metallic characteristics, which was beneficial for electron transport [41, 57]. For the O&Co-defective CoAl-LDHs/ $\text{Ti}_3\text{C}_2\text{O}_2$  composite (Fig. S7C), the  $E_g$  was hardly be



shown because of the overlap of their band structures. Meanwhile, their total density of states (TDOS) and partial density of states (PDOS) were also shown in Fig. S7 and Fig. S8. It was obvious that the CoAl-LDHs systems mainly were composed of O 2s, O 2p and Co 3d orbitals, and the VBM and CBM of CoAl-LDHs mainly were O 2p and Co 3d orbitals, respectively (Fig. S7D and Fig. S8D, E, F). For the  $\text{Ti}_3\text{C}_2\text{O}_2$  (Fig. S7E), the near-Fermi bands of  $\text{Ti}_3\text{C}_2\text{O}_2$  were represented mainly by finite C 2p, O 2p and Ti 3d orbitals. As for the O&Co-defective CoAl-LDHs/ $\text{Ti}_3\text{C}_2\text{O}_2$  composite (Fig. S7F and Fig. S9), the DOS mainly comprised of C 2s, C 2p, O 2s, O 2p, Co 3d, Ti 3d, Ti 4s, Ti 5p and P 3p orbitals. Additionally, the band structure diagram was matched with the DOS diagram as displayed in Fig. S9. The more intensive curve in band structure diagram corresponded to the higher peak intensity in DOS diagram, which signified the more electrons in that, otherwise, the fewer electrons there were. The more electrons could be beneficial to produce more carriers during photocatalytic process [1, 61]. It was obvious that the band structure of defective CoAl-LDHs and CoAl-LDHs/ $\text{Ti}_3\text{C}_2\text{O}_2$  was more intensive than that of perfect CoAl-LDHs, implying it would possess higher photocatalytic performance. Besides, the effective mass of electron is another crucial index to assess the transfer behavior of electrons in materials [64]. According to the calculation, the effective mass of electron for CoAl-LDHs, O-defective CoAl-LDHs, Co-defective CoAl-LDHs and O&Co-defective CoAl-LDHs was 0.175, 0.102, 0.116 and 0.144, respectively. Obviously, the defective systems possessed the smaller effective mass of electron, suggesting the higher mobility of electron. Thus, the separation of photoinduced  $\text{e}^-$ - $\text{h}^+$

pairs and photocatalytic activity would be enhanced in the defective systems [65].

In addition, the optical properties, including dielectric function, absorption coefficient, reflectivity, refractive index, extinction coefficient, loss function and conductivity of the samples had been calculated, which could have important influence on the photocatalytic performance of materials. Firstly, the study of typical optical properties of materials commonly depends on the dielectric function [64]. The complex dielectric function includes two parts:  $\varepsilon(\omega) = \varepsilon_1(\omega) + i\varepsilon_2(\omega)$  ( $\varepsilon_1$  and  $\varepsilon_2$  represents real and imaginary part, respectively), in which the  $\varepsilon_1$  corresponded to the polarization and the  $\varepsilon_2$  explained the energy dissipation in the system [66]. From the real dielectric function ( $\varepsilon_1$ ) (Fig. 8A), it was obvious that the electron polarization existed in the CoAl-LDHs system. Meanwhile, the vacancy would reduce the electron polarization. The  $\varepsilon_2$  of dielectric function was showed in Fig. 8B, for the CoAl-LDHs system, the intensity became slightly higher in the presence of vacancies. As for the  $\text{Ti}_3\text{C}_2\text{O}_2$  and CoAl-LDHs/ $\text{Ti}_3\text{C}_2\text{O}_2$ , a prominent peak was at 4.1 eV. It was worth noting that the composite system exhibited the shift of the absorption peak to the lower energy direction as well as the decreasing sharpness of the peaks, which might be due to the mixed transition and the considerable band gap reduction [66]. Meanwhile, the existence of vacancy and  $\text{Ti}_3\text{C}_2\text{O}_2$  could endow them optically metallic property, which could be beneficial to their photocatalytic activity. The light absorption efficiency performed the significant role in the photocatalytic process, and the calculated absorption coefficient was displayed in Fig. 8C. It was clear that the existence of vacancies could increase the light absorption efficiency to some extent.

Furthermore, the introduction of  $\text{Ti}_3\text{C}_2\text{T}_x$  could significantly increase the light absorption efficiency by CoAl-LDHs. This result was consistent with that of the experiment. The reflectivity coefficients were showed in Fig. 8D. The major peaks of the CoAl-LDHs system located in lower energy region. Since the light reflectivity was positively correlated with the light absorption in the medium, an overall red-shift was produced in the reflectivity spectra of the defective system, thus resulting the narrow of band gap [64]. Meanwhile, the refractive index  $n(\omega)$  and extinction coefficient  $k(\omega)$  for samples were displayed in Fig. 8E, F, clearly, the presence of vacancies and  $\text{Ti}_3\text{C}_2\text{T}_x$  would increase the refractive index of the CoAl-LDHs, thus the CoAl-LDHs/ $\text{Ti}_3\text{C}_2\text{T}_x$  hybrids possessed the higher  $n$  compared to other samples. However, the  $k$  was decreasing in the presence of vacancy and  $\text{Ti}_3\text{C}_2\text{T}_x$ . The higher refractive index and lower extinction coefficient would improve the photocatalytic performance of the material by increasing its utilization of light. The energy loss function corresponding to the energy region, in which the electrons were not typically restricted to their lattice sites and exhibited plasma oscillations upon light irradiation [66]. Meanwhile, the energy loss function could reflect the energy losses by a rapid electron penetrating across the medium. As showed in Fig. 8G, the CoAl-LDHs performed a well-defined abrupt loss peaks at 2.8 eV, however, a lowered loss peaks moved to the lower energy in the defective system, which were associated with the frequency of the plasma resonance. In the  $\text{Ti}_3\text{C}_2\text{T}_x$  system, no obvious loss peak was observed, which should owe to the metallic nature. As for the CoAl-LDHs/ $\text{Ti}_3\text{C}_2\text{T}_x$  sample, the energy loss function was obviously lower than that of CoAl-LDHs system.

The energy loss function spectra indicated that the existence of vacancies and  $\text{Ti}_3\text{C}_2\text{T}_x$  in CoAl-LDHs/ $\text{Ti}_3\text{C}_2\text{T}_x$  system could significantly reduce the energy loss of electrons during photocatalytic process, then improving the photocatalytic performance of CoAl-LDHs/ $\text{Ti}_3\text{C}_2\text{T}_x$  hybrids. The conductivity also had been calculated (Fig. 8H), and it was clear that the introduction of metallic  $\text{Ti}_3\text{C}_2\text{T}_x$  could significantly improve the conductivity of the CoAl-LDHs material, thus accelerating the migration of carriers and improving photocatalytic performance. These calculation results indicated that the introduction of vacancies and  $\text{Ti}_3\text{C}_2\text{T}_x$  materials can improve the optical properties of CoAl-LDHs material, thus improving their photocatalytic performance.

In addition, the work function (WF) of material plays an important role in the study of interfacial charge transfer, and could determine the transfer direction of the photogenerated electrons between the semiconductor and the cocatalyst [21]. As displayed in Fig. S11, the calculated WF of CoAl-LDHs, O-defective CoAl-LDHs, Co-defective CoAl-LDHs, O&Co-defective CoAl-LDHs,  $\text{Ti}_3\text{C}_2\text{O}_2$  and CoAl-LDHs/ $\text{Ti}_3\text{C}_2\text{O}_2$  was 5.91 eV, 5.74 eV, 5.43 eV, 5.09 eV, 4.55 eV and 4.80 eV, respectively. Obviously, the defective CoAl-LDHs systems possessed a lower WF, which meant that the photoinduced electrons in the defective system were more likely to migrate to the surface. Meanwhile, the  $\text{Ti}_3\text{C}_2\text{O}_2$  performed a lower WF than that of CoAl-LDHs systems, suggesting the charges could readily flow from  $\text{Ti}_3\text{C}_2\text{O}_2$  to CoAl-LDHs once contacted [54, 57]. Furthermore, the Fermi level ( $E_F$ ) of samples could be converted by using the following formulas (1-3) [67]. Thus, the  $E_F$  of CoAl-LDHs, O-defective CoAl-LDHs, Co-defective CoAl-LDHs, O&Co-defective

CoAl-LDHs,  $\text{Ti}_3\text{C}_2\text{O}_2$  and O&Co-defective CoAl-LDHs/ $\text{Ti}_3\text{C}_2\text{O}_2$  was 1.00 eV, 0.83 eV, 0.52 eV, 0.18 eV, -0.36 eV and -0.11 eV, respectively.

$$E_F \text{ (vs VAC)} = E_{\text{VAC}} - \text{WF} \dots \dots \dots (1)$$

$$E_F \text{ (vs NHE, pH = 0)} = -4.5 - E_F \text{ (vs VAC)} \dots \dots \dots (2)$$

$$E_F \text{ (vs NHE, pH = 7)} = E_F \text{ (vs NHE, pH = 0)} - 0.059\text{pH} \dots \dots \dots (3)$$

The theoretical results showed that the formation of vacancies and the introduction of  $\text{Ti}_3\text{C}_2\text{T}_x$  MXenes could improve the electronic and optical properties of CoAl-LDHs, which would increase the response to VSL, accelerate charge transfer, reduce  $\text{e}^-$ - $\text{h}^+$  pairs recombination, then increasing the photocatalytic performance of the material, these results were consistent with the experimental results.

### 3.6. Photocatalytic mechanism analysis

For exploring the photocatalytic mechanism, the main active substances during photocatalytic process had been determined via radical trapping tests. As displayed in Fig. 6F, the photocatalytic degradation of TCH was obviously restrained after adding the p-benzoquinone (BQ,  $\cdot\text{O}_2^-$  scavengers) and triethanolamine (TEA,  $\text{h}^+$  scavengers). The photodegradation efficiencies were decreased to 37.87% and 43.21% for BQ and TEA, respectively. It demonstrated that the  $\cdot\text{O}_2^-$  and  $\text{h}^+$  play a significant part in the photocatalysis. For the  $\cdot\text{OH}$  radical, however, only 18.3% efficiency decline in the presence of isopropanol (IPA,  $\cdot\text{OH}$  scavengers), indicating that  $\cdot\text{OH}$  radical was not the main active substances. To verify this point, a  $\text{N}_2$  purging test (excluding  $\text{O}_2$ ) was also performed. These results manifested that the photodegradation performance was

inhibited clearly, affirming the dissolved  $O_2$  performed a significant part for the forming of active substances in the photocatalysis [68]. It could conclude that the  $\cdot O_2^-$ ,  $h^+$ , and  $\cdot OH$  worked together during photocatalytic process, and the ranking of impact was  $\cdot O_2^- > h^+ > \cdot OH$ .

For further verifying the generation of these ROS during photocatalytic process, the EPR spin-trap experiments were performed by using the CALTCT-15 nanohybrid as the photocatalyst under VSL irradiation. As shown in Fig. 9A, there was no obvious characteristic peak appeared for both DMPO- $\cdot O_2^-$  and DMPO- $\cdot OH$  under dark conditions, indicating the active substances could not be generated without light. Furthermore, under VSL illumination, the peak intensity of the DMPO- $\cdot O_2^-$  became greater with longer VSL irradiation, demonstrating the production of the  $\cdot O_2^-$  during photocatalytic process. Meanwhile, the  $\cdot O_2^-$  should be generated from the reduction between photoinduced electron and  $O_2$  due to the potential of the accumulated electrons was more negative than that of the  $O_2$  reduction to  $\cdot O_2^-$  ( $O_2/\cdot O_2^-$ , -0.046 eV) [36]. For the DMPO- $\cdot OH$ , it was obvious that four characteristic peaks (Fig. 9B) appeared under VSL illumination, signifying that the  $\cdot OH$  was also generated. Nevertheless, the VB potential of CoAl-LDHs was more negative than the standard redox potential of  $OH^-/\cdot OH$  (2.40 eV) and  $H_2O/\cdot OH$  (2.72 eV) [36], therefore the pathway to generate  $\cdot OH$  by the oxidization of  $H_2O$  was thermodynamically improbable. Based on previous studies, another pathway could also be activated to generate  $\cdot OH$ , namely, the  $O_2$  catch the photoinduced electron to form  $\cdot O_2^-$  and then producing the  $\cdot OH$  [61]. Furthermore, the concentration of  $\cdot OH$  and  $\cdot O_2^-$  on different

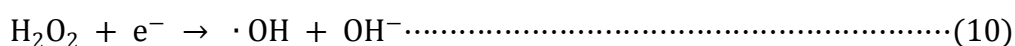
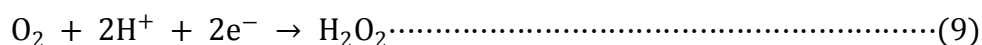
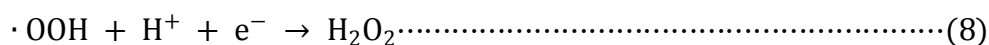
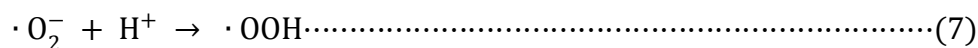
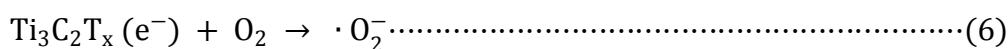
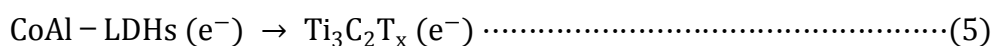
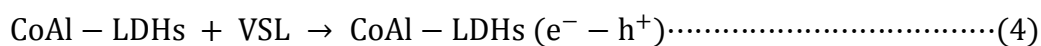
catalysts was further estimated by using the coumarin and nitroblue tetrazolium (NBT) as the probe, respectively [69-74] (The details were shown in the supplementary information). As displayed in Fig. 9C, the spectra of 7-hydroxycoumarin showed the different fluorescence intensity on different photocatalyst, indicating the different  $\cdot\text{OH}$  concentration on different photocatalyst [69-71]. Meanwhile, the transformation percentage of NBT was also different in different photocatalytic systems (Fig. 9D), representing the different  $\cdot\text{O}_2^-$  concentration in different photocatalytic systems [72-74]. However, compared with other photocatalysts, the CALTCT-15 sample showed the highest fluorescence intensity and the NBT transformation percentage, which means that the higher  $\cdot\text{OH}$  and  $\cdot\text{O}_2^-$  concentration in this photocatalytic system, thus endowing the higher photocatalytic performance, the results were consistent with the above photodegradation results [69, 72, 75].

Based on the above experimental and theoretical results, a probable photodegradation mechanism was proposed in Fig. 10. Under VSL irradiation, the photoinduced electrons migrated from the VB to the CB of the CoAl-LDHs nanosheets. Before contact, the  $E_F$  is the chemical potential of thermodynamic equilibrium, the  $E_F$  of O&Co-defective CoAl-LDHs was 0.18 eV [76], and the  $E_F$  of  $\text{Ti}_3\text{C}_2\text{T}_x$  was about -0.36 eV. However, after contact, the electrons in  $\text{Ti}_3\text{C}_2\text{T}_x$  with a low WF flow into CoAl-LDHs with a high WF. Then, the CoAl-LDHs layer would gather negative charge, meanwhile, the  $\text{Ti}_3\text{C}_2\text{T}_x$  layer would accumulate positive charge. Finally, the two  $E_F$  achieved equilibrium and this spontaneous interfacial charge transfer will lead to the formation of an internal electric field at the interface

[21, 77]. As a result, the internal electric field between interfaces could restrain the recombination of  $e^-h^+$  pairs, thus increasing the chance of the photoinduced  $e^-$  and  $h^+$  to take part in the redox reaction on the surface [21, 78]. Meanwhile, the energy bands of CoAl-LDHs would shift upward by 0.29 eV along with the  $E_F$ . Therefore, the new CB of CoAl-LDHs (-1.03 eV) is more negative than the new  $E_F$  of  $Ti_3C_2T_x$  (-0.11 eV), and the photoinduced electrons could transfer from CoAl-LDHs to  $Ti_3C_2T_x$ . Furthermore, the CB and VB of CoAl-LDHs were bent upward after contacted with metallic  $Ti_3C_2T_x$ , resulting in the forming of Schottky junction at the interface, the existing of Schottky barrier would prevent the electrons from diffusing back to the CoAl-LDHs [21, 79, 80]. Thus, the excellent electron mobility of  $Ti_3C_2T_x$  could serve as an electron trapping and shuttling site, which was beneficial for accelerating the electrons transfer and subsequently suppress the recombination of photoexcited  $e^-h^+$  pairs, leading to the increase in the number of  $e^-$  and  $h^+$  participating in the photocatalytic reaction [6, 7, 21, 22]. Besides, the new vacancy energy levels could be produced due to the rich O and Co vacancies ( $V_O$  and  $V_{Co}$ ), which could enhance VSL absorption, meanwhile, the rich vacancies could also be as electron acceptors and the temporary traps of electrons in CoAl-LDHs nanostructures, thus reducing the recombination of  $e^-h^+$  pairs further [13]. Finally, the accumulated electrons quickly transfer to the surface of  $Ti_3C_2T_x$  due to the excellent metallic conductivity, and could reduce  $O_2$  to generate  $\cdot O_2^-$  due to the  $E_F$  of  $Ti_3C_2T_x$  (-0.11 eV) was more negative than the potential of  $O_2/\cdot O_2^-$  (-0.046 eV). In the meantime, the generated  $\cdot O_2^-$  could further be reduced to generate  $\cdot OH$ . In addition, the  $\cdot OH$  could also be produced in the



multiple electron reduction reactions ( $O_2 \rightarrow H_2O_2 \rightarrow \cdot OH$ ) due to the strong redox reactivity of the naked Ti sites on the surface of  $Ti_3C_2T_x$  [26]. These strong oxidized radicals ( $h^+$ ,  $\cdot O_2^-$ ,  $\cdot OH$ ) ultimately degrade antibiotic into  $CO_2$ ,  $H_2O$  or others. The mainly possible reactions for the antibiotic photodegradation were showed as follows:



#### 4. Conclusions

A hybrid 2D/2D CoAl-LDHs/ $Ti_3C_2T_x$  photocatalysts were prepared by co-assembly of exfoliated CoAl-LDHs and  $Ti_3C_2T_x$  nanosheets. Variety characterization techniques revealed that the ultrathin CoAl-ELDHD nanosheets contained about four host layers ( $\sim 3.2$  nm) and they were porous accompany with rich O and Co vacancies. Meanwhile, the  $Ti_3C_2T_x$  nanosheets were determined about three layers ( $\sim 5.1$  nm). The photocatalytic degradation experiments manifested that the optimized CALTCT-15 nanohybrid performed excellent VSL photocatalytic ability towards TCH removal, which were 2.62 folds higher than that of pure CoAl-LDHs.

The excellent photocatalytic activity should be attributed to the synergistic effect, the porous and rich vacancies, and the Schottky junction formed of CoAl-LDHs and  $\text{Ti}_3\text{C}_2\text{T}_x$ , which endowed the hybrid excellent physico-chemical and optical-electrical properties, thus possess well VSL absorption, high specific surface area, rapid electrons transfer and depressed electron-hole pairs recombination. Further, the theoretical calculations had verified these merits of CoAl-LDHs/ $\text{Ti}_3\text{C}_2\text{T}_x$  nanohybrids based on the calculated electrical and optical characteristics (including band structures, density of states, effective mass of electron, dielectric function, absorption coefficient, reflectivity, refractive index, extinction coefficient, loss function, conductivity and work function). This study would stimulate some new ideas in employing LDHs and MXenes to build the novel and efficient heterostructure photocatalysts for environmental remediation and some other applications.

## **Acknowledgments**

The study was financially supported by the Program for Changjiang Scholars and Innovative Research Team in University (IRT-13R17), the National Natural Science Foundation of China (51979103, 51679085, 51521006, 51508177), the Fundamental Research Funds for the Central Universities of China (531107050930), the Funds of Hunan Science and Technology Innovation Project (2018RS3115). The authors also gratefully acknowledge the National Supercomputing Center in Changsha for providing the computing resources.

## References

- [1] B. Shao, X. Liu, Z. Liu, G. Zeng, Q. Liang, C. Liang, Y. Cheng, W. Zhang, Y. Liu, S. Gong, *Chemical Engineering Journal* 368 (2019) 730-745.
- [2] Y. Liu, M. Cheng, Z. Liu, G. Zeng, H. Zhong, M. Chen, C. Zhou, W. Xiong, B. Shao, B. Song, *Chemosphere* 236 (2019) 124387.
- [3] J. Chen, Z. He, G. Li, T. An, H. Shi, Y. Li, *Applied Catalysis B: Environmental*, 209 (2017) 146-154.
- [4] T. An, J. Chen, X. Nie, G. Li, H. Zhang, X. Liu, H. Zhao, *ACS Applied Materials & Interfaces*, 4 (2012) 5988-5996.
- [5] W. Yuan, L. Cheng, Y. Zhang, H. Wu, S. Lv, L. Chai, X. Guo, L. Zheng, *Advanced Materials Interfaces* 4 (2017) 1700577.
- [6] J. Chen, H. Zhang, P. Liu, Y. Li, X. Liu, G. Li, P.K. Wong, T. An, H. Zhao, *Applied Catalysis B: Environmental*, 168-169 (2015) 266-273.
- [7] P. Wei, D. Qin, J. Chen, Y. Li, M. Wen, Y. Ji, G. Li, T. An, *Environmental Science: Nano*, 6 (2019) 959-969.
- [8] W.K. Jo, S. Tonda, *Journal of Hazardous Materials* 368 (2019) 778-787.
- [9] H. Huang, Y. Song, N. Li, D. Chen, Q. Xu, H. Li, J. He, J. Lu, *Applied Catalysis B: Environmental* 251 (2019) 154-161.
- [10] Y. Wu, H. Wang, Y. Sun, T. Xiao, W. Tu, X. Yuan, G. Zeng, S. Li, J.W. Chew, *Applied Catalysis B: Environmental* 227 (2018) 530-540.
- [11] J. Zou, Z. Wang, W. Guo, B. Guo, Y. Yu, L. Wu, *Applied Catalysis B: Environmental* 260 (2020) 118185.
- [12] S. Kumar, M.A. Isaacs, R. Trofimovaite, L. Durndell, C.M.A. Parlett, R.E. Douthwaite, B. Coulson, M.C.R. Cockett, K. Wilson, A.F. Lee, *Applied Catalysis B: Environmental* 209 (2017) 394-404.
- [13] X. Hao, Y. Wang, J. Zhou, Z. Cui, Y. Wang, Z. Zou, *Applied Catalysis B: Environmental* 221 (2018) 302-311.
- [14] K. Wang, C. Miao, Y. Liu, L. Cai, W. Jones, J. Fan, D. Li, J. Feng, *Applied Catalysis B: Environmental*, 270 (2020) 118878.
- [15] Z. Wang, Y. Song, J. Zou, L. Li, W. Ling, *Catalysis Science & Technology* 8 (2017) 420-429.
- [16] N. Michael, K. Murat, P. Volker, L. Jun, N. Junjie, H. Min, H. Lars, G. Yury, M.W. Barsoum, *Advanced Materials* 23 (2011) 4248-4253.
- [17] J. Peng, X. Chen, W.-J. Ong, X. Zhao, N. Li, *Chem* 5 (2019) 18-50.
- [18] Y. Sun, D. Jin, Y. Sun, X. Meng, Y. Gao, Y. Dall'Agnese, G. Chen, X.-F. Wang, *Journal of Materials Chemistry A* 6 (2018) 9124-9131.
- [19] B. Shao, Z. Liu, G. Zeng, H. Wang, Q. Liang, Q. He, M. Cheng, C. Zhou, L. Jiang, B. Song, *Journal of Materials Chemistry A* 8 (2020) 7508-7535.
- [20] H. Wang, Y. Wu, X. Yuan, G. Zeng, J. Zhou, X. Wang, J.W. Chew, *Advanced Materials* 30 (2018) e1704561.
- [21] Y. Liu, Y.H. Li, X. Li, Q. Zhang, H. Yu, X. Peng, F. Peng, *ACS Nano*, 14 (2020) 14181-14189.
- [22] B. Shao, J. Wang, Z. Liu, G. Zeng, L. Tang, Q. Liang, Q. He, T. Wu, Y. Liu, X. Yuan, *Journal of Materials Chemistry A*, 8 (2020) 5171-5185.
- [23] X. Yi, J. Yuan, H. Tang, Y. Du, B. Hassan, K. Yin, Y. Chen, X. Liu, *Journal of colloid and interface science*, 571 (2020) 297-306.

- [24] G. Zuo, Y. Wang, W.L. Teo, A. Xie, Y. Guo, Y. Dai, W. Zhou, D. Jana, Q. Xian, W. Dong, Y. Zhao, *Angewandte Chemie International Edition*, 59 (2020) 11287-11292.
- [25] T. Su, Z.D. Hood, M. Naguib, L. Bai, S. Luo, C.M. Rouleau, I.N. Ivanov, H. Ji, Z. Qin, Z. Wu, *Nanoscale* 11 (2019) 8138-8149.
- [26] T. Cai, L. Wang, Y. Liu, S. Zhang, W. Dong, H. Chen, X. Yi, J. Yuan, X. Xia, C. Liu, S. Luo, *Applied Catalysis B: Environmental* 239 (2018) 545-554.
- [27] X. Shuaikai, D.A. Yohan, W. Guodong, Z. Chao, G. Yury, H. Wei, *Nano Energy*, 50 (2018) 479-488.
- [28] L. Hu, M. Li, X. Wei, H. Wang, C. Zhu, *Chemical Engineering Journal*, 398 (2020) 125605.
- [29] D. Zhang, J. Cao, X. Zhang, N. Insin, S. Wang, Y. Zhao, J. Qin, *ACS Applied Energy Materials*, 3 (2020) 11119-11130.
- [30] C. Sun, P. Zuo, W. Sun, R. Xia, Z. Dong, L. Zhu, J. Lv, G. Deng, L. Tan, Y. Dai, *ACS Applied Energy Materials*, 3 (2020) 10242-10254.
- [31] M. Yu, S. Zhou, Z. Wang, J. Zhao, J. Qiu, *Nano Energy*, 44 (2018) 181-190.
- [32] Q. Wang, L. Chen, S. Guan, X. Zhang, B. Wang, X. Cao, Z. Yu, Y. He, D.G. Evans, J. Feng, D. Li, *ACS Catalysis* 8 (2018) 3104-3115.
- [33] B. Shao, Z. Liu, G. Zeng, Z. Wu, Y. Liu, M. Cheng, M. Chen, Y. Liu, W. Zhang, H. Feng, *ACS Sustainable Chemistry & Engineering*, 6 (2018) 16424-16436.
- [34] A. Lipatov, M. Alhabeb, M.R. Lukatskaya, A. Boson, Y. Gogotsi, A. Sinitskii, *Advanced Electronic Materials* 2 (2016) 1600255.
- [35] Y. Tang, H. Shen, J. Cheng, Z. Liang, C. Qu, H. Tabassum, R. Zou, *Advanced Functional Materials*, 30 (2020) 1908223.
- [36] H. Wang, Y. Wu, T. Xiao, X. Yuan, G. Zeng, W. Tu, S. Wu, H.Y. Lee, Y.Z. Tan, J.W. Chew, *Applied Catalysis B: Environmental*, 233 (2018) 213-225.
- [37] C. Peng, P. Wei, X. Li, Y. Liu, Y. Cao, H. Wang, H. Yu, F. Peng, L. Zhang, B. Zhang, K. Lv, *Nano Energy*, 53 (2018) 97-107.
- [38] D.A. Islam, K. Barman, S. Jasimuddin, H. Acharya, *Nanoscale*, 11 (2019) 7560-7566.
- [39] R. Ahmad, R. Kumar, *Journal of Environmental Management* 91 (2010) 1032-1038.
- [40] Y. Zhang, D. Du, X. Li, H. Sun, L. Li, P. Bai, W. Xing, Q. Xue, Z. Yan, *ACS Applied Materials & Interfaces* 9 (2017) 31699-31709.
- [41] Z. Zeng, Y. Yan, J. Chen, P. Zan, Q. Tian, P. Chen, *Advanced Functional Materials* 29 (2019) 1806500.
- [42] L. Zhang, K.N. Hui, K.S. Hui, H. Lee, *Electrochim. Acta*, 186 (2015) 522-529.
- [43] Y. Chen, C. Jing, X. Zhang, D. Jiang, X. Liu, B. Dong, L. Feng, S. Li, Y. Zhang, *Journal of colloid and interface science* 548 (2019) 100-109.
- [44] H. Niu, X. Yang, Q. Wang, X. Jing, K. Cheng, K. Zhu, K. Ye, G. Wang, D. Cao, J. Yan, *Journal of Energy Chemistry* 46 (2020) 105-113.
- [45] P.F. Liu, S. Yang, B. Zhang, H.G. Yang, *ACS Applied Materials & Interfaces*, 8 (2016) 34474-34481.
- [46] H. Wang, Y. Yuan, J. Gu, Z. Jia, Z. Lu, Z. Bai, L. Yang, X. Yang, *Journal of Power Sources*, 467 (2020) 228354.
- [47] R. Zhang, Y. C. Zhang, L. Pan, G. Q. Shen, N. Mahmood, Y. H. Ma, Y. Shi, W. Jia, L. Wang, X. Zhang, W. Xu, J. J. Zou, *ACS Catalysis*, 8 (2018) 3803-3811.
- [48] L. Pan, S. Wang, W. Mi, J. Song, J. J. Zou, L. Wang, X. Zhang, *Nano Energy*, 9 (2014) 71-79.
- [49] X. Liu, L. Zhao, H. Xu, Q. Huang, Y. Wang, C. Hou, Y. Hou, J. Wang, F. Dang, J. Zhang, *Advanced Energy Materials*, 10 (2020) 2001415.

809 [50] R. Gao, Z. Shang, L. Zheng, J. Wang, L. Sun, Z. Hu, X. Liu, *Inorganic Chemistry*, 58 (2019)  
810 4989-4996.

811 [51] H. Liang, H. Jia, T. Lin, Z. Wang, C. Li, S. Chen, J. Qi, J. Cao, W. Fei, J. Feng, *Journal of colloid and*  
812 *interface science*, 554 (2019) 59-65.

813 [52] P. Tian, X. He, L. Zhao, W. Li, W. Fang, H. Chen, F. Zhang, Z. Huang, H. Wang, *International Journal*  
814 *of Hydrogen Energy* 44 (2019) 788-800.

815 [53] C. Peng, X. Yang, Y. Li, H. Yu, H. Wang, F. Peng, *ACS Applied Materials & Interfaces* 8 (2016)  
816 6051-6060.

817 [54] H. Wang, Y. Sun, Y. Wu, W. Tu, S. Wu, X. Yuan, G. Zeng, Z.J. Xu, S. Li, J.W. Chew, *Applied Catalysis B:*  
818 *Environmental* 245 (2019) 290-301.

819 [55] Y. Li, Z. Yin, G. Ji, Z. Liang, Y. Xue, Y. Guo, J. Tian, X. Wang, H. Cui, *Applied Catalysis B:*  
820 *Environmental* 246 (2019) 12-20.

821 [56] L. Tan, S.-M. Xu, Z. Wang, Y. Xu, X. Wang, X. Hao, S. Bai, C. Ning, Y. Wang, W. Zhang, Y.K. Jo, S.-J.  
822 Hwang, X. Cao, X. Zheng, H. Yan, Y. Zhao, H. Duan, Y.-F. Song, *Angewandte Chemie International Edition*  
823 131 (2019) 11986-11993.

824 [57] J. Ran, G. Gao, F.T. Li, T.Y. Ma, A. Du, S.Z. Qiao, *Nature Communications* 8 (2017) 13907.

825 [58] J. Ke, J. Liu, H. Sun, H. Zhang, X. Duan, P. Liang, X. Li, M.O. Tade, S. Liu, S. Wang, *Applied Catalysis B:*  
826 *Environmental* 200 (2017) 47-55.

827 [59] W. Chen, B. Han, Y. Xie, S. Liang, H. Deng, Z. Lin, *Chemical Engineering Journal*, 391 (2020) 123519.

828 [60] J. H. Zhao, L. W. Liu, K. Li, T. Li, F. T. Liu, *CrystEngComm* 21 (2019) 2416-2421.

829 [61] B. Shao, X. Liu, Z. Liu, G. Zeng, W. Zhang, Q. Liang, Y. Liu, Q. He, X. Yuan, D. Wang, S. Luo, S. Gong,  
830 *Chemical Engineering Journal* 374 (2019) 479-493.

831 [62] S. Gao, B. Gu, X. Jiao, Y. Sun, X. Zu, F. Yang, W. Zhu, C. Wang, Z. Feng, B. Ye, Y. Xie, *Journal of the*  
832 *American Chemical Society* 139 (2017) 3438-3445.

833 [63] J. Xiong, J. Di, J. Xia, W. Zhu, H. Li, *Advanced Functional Materials* 28 (2018) 1801983.

834 [64] Q. Zhang, X. Chen, W.-C. Liu, Y. Wang, *Computational Materials Science* 158 (2019) 272-281.

835 [65] Y. C. Zhang, Z. Li, L. Zhang, L. Pan, X. Zhang, L. Wang, A. Fazal e, J. J. Zou, *Applied Catalysis B:*  
836 *Environmental* 224 (2018) 101-108.

837 [66] M. Rizwan, A. Ali, Z. Usman, N.R. Khalid, H.B. Jin, C.B. Cao, *Physica B*, 552 (2019) 52-57.

838 [67] S. Cao, B. Shen, T. Tong, J. Fu, J. Yu, *Advanced Functional Materials* 28 (2018) 1800136.

839 [68] F. Chen, Q. Yang, X. Li, G. Zeng, D. Wang, C. Niu, J. Zhao, H. An, T. Xie, Y. Deng, *Applied Catalysis B:*  
840 *Environmental* 200 (2017) 330-342.

841 [69] Q. Xiang, J. Yu, P.K. Wong, *Journal of colloid and interface science*, 357 (2011) 163-167.

842 [70] S.J. De-Nasri, S. Nagarajan, P.K.J. Robertson, V.V. Ranade, *Chemical Engineering Journal*, (2020)  
843 127560.

844 [71] V. Leandri, J.M. Gardner, M. Jonsson, *The Journal of Physical Chemistry C*, 123 (2019) 6667-6674.

845 [72] L. Ye, J. Liu, C. Gong, L. Tian, T. Peng, L. Zan, *ACS Catalysis*, 2 (2012) 1677-1683.

846 [73] L. Ye, J. Liu, Z. Jiang, T. Peng, L. Zan, *Applied Catalysis B: Environmental*, 142-143 (2013) 1-7.

847 [74] S. Obregon, M.A. Ruiz-Gomez, D.B. Hernandez-Uresti, *Journal of colloid and interface science*, 506  
848 (2017) 111-119.

849 [75] Y. Nosaka, A.Y. Nosaka, *Chemical Reviews*, 117 (2017) 11302-11336.

850 [76] S. Das, S. Patnaik, K.M. Parida, *Inorganic Chemistry Frontiers* 6 (2019) 94-109.

851 [77] R.K. Chava, J.Y. Do, M. Kang, *Journal of Materials Chemistry A* 7 (2019) 13614-13628.

852 [78] Y. Chen, T. Shi, P. Liu, X. Ma, L. Shui, C. Shang, Z. Chen, X. Wang, K. Kempa, G. Zhou, *Journal of*

853 Materials Chemistry A 6 (2018) 19167-19175.  
854 [79] R. Xiao, C. Zhao, Z. Zou, Z. Chen, L. Tian, H. Xu, H. Tang, Q. Liu, Z. Lin, X. Yang, Applied Catalysis B:  
855 Environmental 268 (2020) 118382.  
856 [80] B. Li, S. Liu, C. Lai, G. Zeng, M. Zhang, M. Zhou, D. Huang, L. Qin, X. Liu, Z. Li, N. An, F. Xu, H. Yi, Y.  
857 Zhang, L. Chen, Applied Catalysis B: Environmental 266 (2020) 118650.  
858